URMC-099 Prophylaxis Repairs Hippocampal Vascular Damage in an Orthopedic Model of Delirium Superimposed on Dementia

Patrick Miller-Rhodes[1,2*], Herman Li[1*], Ravikanth Velagapudi[3], Niccolò Terrando[3,4,5**], Harris A Gelbard[1,6,7,8,9]

[1,2*]Patrick Miller-Rhodes, [1]Center for Neurotherapeutics Discovery, [2]Neuroscience Graduate Program, University of Rochester Medical Center, Rochester, NY

[1*]Herman Li, Center for Neurotherapeutics Discovery, Department of Neurology, University of Rochester Medical Center, Rochester, NY

[3]Ravikanth Velagapudi, Department of Anesthesiology, Duke University Medical Center, Durham, NC

[3,4,5**]Niccolò Terrando, Department of Anesthesiology, [4]Cell Biology, and [5]Immunology, Duke University Medical Center, Durham, NC

[1,6,7,8,9]Harris A Gelbard, [1]Center for Neurotherapeutics Discovery, [6]Department of Neurology, [7]Department of Neuroscience, [8]Department of Pediatrics, [9]Department of Microbiology & Immunology, University of Rochester Medical Center, Rochester, NY

[*]Patrick Miller-Rhodes and Herman Li contributed to this work equally.

[**]Address correspondence to Niccolò Terrando: niccolo.terrando@duke.edu

Abstract

Systemic perturbations can drive a neuroimmune cascade after surgical trauma, including affecting the blood-brain barrier (BBB), activating microglia, and contributing to cognitive deficits such as delirium. Delirium superimposed on dementia (DSD) is a particularly debilitating complication that renders the brain further vulnerable to neuroinflammation and neurodegeneration, albeit these molecular mechanisms remain poorly understood. Here we have used an orthopedic model of tibial fracture/fixation in APPSwDI/mNos2$^{-/-}$ AD (CVN-AD) mice to investigate relevant pathogenetic mechanisms underlying DSD. We conducted the present study in 6 months-old CVN-AD mice, an age at which we speculated amyloid-β pathology had not saturated BBB and neuroimmune functioning. We found that URMC-099, our brain-penetrant anti-inflammatory neuroprotective drug, prevented inflammatory endothelial activation, synapse loss, and microglial activation in our DSD model. Taken together, our data link post-surgical endothelial activation, microglial MafB immunoreactivity, and synapse loss as key substrates for DSD, all of which can be reversed by URMC-099.

Key words: blood-brain barrier (BBB), CVN-AD, delirium superimposed on dementia (DSD), leucine rich repeat kinase type 2 (LRRK2), microgliosis, mixed lineage kinase type 3 (MLK3), neuroinflammation, URMC-099, vascular cell adhesion molecule type 1 (VCAM-1)

Introduction

Vascular etiologies for cognitive impairment and dementia are a growing research interest, yet the impact of systemic stressors on the neurovascular unit (NVU) is far less established, especially in the context of perioperative complications. Neurologic sequelae following routine surgeries are common, can accelerate neurodegenerative processes, and contribute to significant mortality. Indeed, patients with Alzheimer's disease (AD) often require orthopedic surgery to repair a broken limb and become particularly vulnerable to complications, including postoperative delirium (POD), an acute state of cognitive impairment that develops in the hospital setting [1-3]. POD is associated with an increased one-year mortality and a worsening of cognitive trajectories in patients with pre-existing neurodegeneration [4, 5]. Despite the prevalence of POD in this population, the pathophysiology of delirium superimposed on dementia (DSD) remains poorly understood and without disease-modifying or prophylactic therapeutic interventions.

To better understand the underlying etiology we started to characterize the neurovascular and immunological sequelae in a model of DSD following tibial fracture and fixation in 12 months-old CVN-AD mice [6]. In the absence of surgical manipulation, the CVN-AD model displays age-dependent effects including amyloid-β accumulation [7], cerebral amyloid angiopathy (CAA), tau phosphorylation [7-9], microgliosis [7], astrogliosis [8], neurovascular unit dysfunction [10], increased expression of complement components [8], and neuronal degeneration [9]. For the present study, we chose 6-months-old mice to determine whether this intermediate prodromal time point would allow therapeutic intervention with URMC-099. In our prior work we have established that tibial fracture/fixation in this mouse accelerates neurodegenerative pathology, especially

amyloid-β accumulation in the dentate gyrus (DG) region of hippocampus, which is accompanied by delirium-like behavior as defined by inattention deficits in the 5-choice serial reaction time task [6]. Because vascular factors, including vascular cell adhesion molecule type 1 (VCAM-1), have been identified in a proteomics screen as key gateway proteins associated with pathologic aging [11], we sought to investigate whether surgery impacted VCAM-1 expression and whether treatment with URMC-099 in CVN-AD could reverse neurovascular pathology in DSD. We focused our investigation on the stratum lacunosum-moleculare (SLM) layer of CA1 vs. the DG because of its unique vulnerability to BBB dysfunction [12] and synaptic degeneration [13] — two key therapeutic targets of URMC-099 in mouse models of neurodegeneration and neuroinflammation [14-16].

Materials and methods

Cell culture

Bend.3 cells [17] (ATCC CRL-2299; BALB/c origin; generously provided by Dr. Ning Quan) were cultured in glutamate-free Dulbecco's Modified Eagle's Medium (DMEM) supplemented with GlutaMAX (1% v/v) and fetal bovine serum (FBS; 10% v/v) and maintained in a humidified 37° C incubator (5% CO2). For immunocytochemistry (ICC), bend.3 cells were seeded at a density of 100,000 cells per well on plasma-cleaned, poly-D-lysine-coated coverslips in a 12-well plate and allowed to adhere overnight. Subsequently, bend.3 cells were serum starved for 30 minutes, followed by addition of URMC-099 (300 nM in DMSO). Thirty minutes after URMC-099 pre- treatment, PBS or IL-1β (10 ng/mL) was added as indicated. Bend.3 cells were fixed 16 hr post-IL-1β stimulation for ICC. For quantitative reverse-transcriptase polymerase chain reaction (qRT-PCR), bend.3 cells were treated exactly as above, except cells were seeded at

200,000 cells per 12-well and lysates were collected at 6 hr post-IL-1β stimulation.

Animals and orthopedic surgery

APPSwDI/mNos2$^{-/-}$ AD mice (CVN-AD; kindly provided by Dr. Carol Colton, Duke University) were bred and maintained by the Terrando laboratory at Duke University. The procedures followed to provide tissues from APPSwDI/mNos2$^{-/-}$ AD mice were performed in strict compliance with animal protocols approved by the Institutional Animal Care and Use Committees (IACUC) of Duke University (A249-17-11). Mice were housed under a 12-hr light/dark cycle with free access to water and regular chow. URMC-099 prophylaxis and orthopedic surgery were performed as described in Miller-Rhodes et al., 2019 [16] on 6-month of APPSwDI/mNos2$^{-/-}$ mice under isoflurane (Patterson Veterinary, Greeley, CO) anesthesia and analgesia (buprenorphine, 0.1 mg/kg subcutaneously; ZooPharm, Laramie, WY). All mice recovered from surgery and were included in the study.

Immunocytochemistry

Immunocytochemistry was performed per Glynn et al., 2006's protocol [18] with minor modifications. Briefly, following fixation in 4% PFA/4% sucrose solution for 15 min at 4°C, cells were washed with 100 nM glycine (in 1X PBS), followed by two more washes in 1X PBS. Cells were permeabilized in 0.25% Triton-X for 5 min (followed by 2 PBS washes), blocked in 10% bovine serum albumin (BSA) in 1X PBS, and incubated with primary antibodies in 3% BSA for 1 hr at room temperature. Primary antibodies included rat monoclonal anti-VCAM1 (Abcam, ab19569, clone M/K-2; 1:250) and Armenian hamster anti-PECAM-1 (CD31; Millipore Sigma, cat no. MAB1398Z, clone 2H8; 1:250). Cells were washed again three times with 1X PBS and incubated with secondary antibodies in 3%

BSA for 45 min at room temperature. Cells were washed a final three times with 1X PBS, dipped in ddH20 to remove excess salt, and mounted on microscope slides with Prolong Diamond anti-fade reagent (ThermoFisher, cat no. P36961).

Quantitative reverse transcriptase polymerase chain reaction (qRT-PCR)

RNA was extracted using a spin column RNA isolation kit (Machery-Nagel). On-column DNase treatment was used to remove contaminating genomic DNA. Total RNA preparations were then used directly for qPCR (200 ng total RNA per reaction) using the Luna Universal One-Step RT-qPCR Kit (NEB, E3006) and target-specific primer/probe sets (ThermoFisher) or frozen at -80° C until use. The qPCR primer/probe sets we used include the endogenous control *Ipo8* (Mm01255158_m1), *Vcam1* (Mm01320970_m1), *Spp1* (Mm00436767_m1), *Timp1* (Mm01341361_m1), and *Col1a1* (Mm00801666_g1). The ΔΔCt method was used to analyze the results.

Immunohistochemistry

Twenty-four hours after orthopedic surgery, mice were deeply anesthetized with isoflurane and transcardially perfused with PBS and subsequently 4% PFA. Brains were carefully extracted and post-fixed for 24 hr in 4% PFA. Brains were transferred to conical tubes containing PBS, packed with ice-packs, and shipped to the Gelbard laboratory at University of Rochester Medical Center. Coronal brain sections (40 μm thickness) were cut using a vibratome and stored in cryoprotectant (30% PEG300, 30% glycerol, 20% 0.1 M phosphate buffer, and 20% ddH2O) at -20˚ C. For immunohistochemistry, cryopreserved sections were washed three times in 1X PBS followed by another wash in 0.1 M glycine in 1X PBS (to reduce autofluorescence). Sections were subsequently

incubated in blocking buffer (1.5% BSA, 3% normal goat serum, 0.5% Triton-X, and 1.8% NaCl in 1X PBS) containing primary antibodies (VCAM1 Millipore Sigma MAB1398Z 1:200; Tmem119 SySy 1:500; Iba1 Wako PTR2404 1:1000; MafB Atlas HPA005653 1:500; CD68 Serotec MCA1957GA 1:1000; Homer1 SySy 160006 1:500; PSD95 NeuroMab 75-028 1:500; Piccolo SySy 142104 1:500; C1q Abcam AB71940 1:500) in blocking buffer (1.5% BSA, 3% normal goat serum, 0.5% Triton-X, and 1.8% NaCl in 1X PBS) overnight at room temperature. Then sections were washed thrice in 1X PBS containing 1.8% NaCl before incubating in Alexa Fluor conjugated secondary antibodies (ThermoFisher), again overnight. Finally, sections were washed three times with 1X PBS+1.8% NaCl, mounted on glass slides, and cover-slipped with Prolong Diamond Antifade Reagent (Invitrogen P36961). When used, the UV-excitable fibrillar amyloid-β dye Amylo-Glo (Biosensis TR-300-AG; 1:100) or Alexa-633 Hydrazide (Thermo Fisher A30634; 1:1000) was diluted in 1X PBS+1.8% NaCl and applied to sections for 10 min following the first two post-secondary washes; an additional two washes (1X PBS+1.8% NaCl) were performed to rinse the sections of excess Amylo-Glo dye or Alexa-633 Hydrazide.

Grid pseudo-confocal microscopy and image analysis

Slides were coded throughout imaging and analysis to reduce experimenter bias. We used an Olympus BX-51 microscope equipped with Quioptic Optigrid hardware (for optical sectioning) and a Hamamatsu ORCA-ER camera. Images were acquired using Volocity 3DM software (Quorum Technologies). Within each set, light intensity and exposure settings were kept constant. For ICC, three images were acquired for each experimental replicate. For IHC, six images were acquired for each biological replicate.

Synaptic punctae were imaged at 60X magnification (10μm depth, 0.3μm step size). To reduce variability due to differences in vascular coverage (i.e., areas without synaptic punctae), we selected 300 x 300 pixel ROIs from each XYZ-stack for analysis. Other markers were imaged at 20X and 40X magnification. Immunostained objects were identified and quantified using custom Volocity workflows. More specifically, for synaptic punctae, the colocalization of spots and objects were used to identify punctae. The "Find Spots" function was used to identify individual puncta based on local intensity maxima and "Find Objects" function was used to identify punctae with a minimum intensity threshold; all other quantified objects were identified using the "Find Objects" function. Arterial VCAM-1 vessels were defined as VCAM-1 objects touching Alexa-633 objects. Tmem119^{lo} and Tmem119^{hi} Iba1-positive cells were determined by intensity thresholding (by standard deviation; SD = 1.2). Microglial MafB intensity was quantified as the sum intensity of MafB objects contained within Iba1-positive objects and normalized to the number of microglia in each field of view. Non-microglial MafB was quantified as the sum intensity of MafB objects *not* contained within Iba1-positive objects and normalized to the number of MafB+ nuclei per field. Microglial CD68 was quantified as the sum intensity of CD68 objects contained with Iba1-positive objects.

Statistics

All qPCR statistics were performed on ΔCt values and then represented graphically as fold change ($2^{-\Delta\Delta Ct}$). One- and two-way analysis of variance (ANOVA) with Holm-Sidak's or Tukey's multiple comparison tests were used to analyze the ICC and IHC data as indicated in each figure legend. Pearson's correlation was used to compute correlations between VCAM-1 immunoreactivity and fibrillar amyloid-β volume. All data are presented

as mean ± standard error (SEM) with significance at $P < 0.05$.

Results

Effect of URMC-099 on brain endothelial cell activation in vitro

Although URMC-099's pharmacokinetic properties allow it to readily cross the BBB and achieve therapeutic concentrations in the CNS to act directly on microglia, its therapeutic efficacy in *in vivo* models of systemic inflammation may be attributable, at least in part, to actions on the cerebrovascular endothelium. To test whether URMC-099 can inhibit the activation of brain endothelial cells (BECs) under inflammatory conditions, we analyzed VCAM-1 and PECAM-1 (CD31) immunoreactivity (IR) on bend.3 cells, a murine cerebral microvascular endothelial cell line [17], following stimulation with the pro-inflammatory cytokine IL-1β (10 ng/mL) alone or in combination with URMC-099 (300 nM). Twenty-four hours following IL-1β stimulation, bend.3 cells upregulated VCAM-1 ($p = 0.0003$), but not PECAM-1 immunoreactivity (IR) (**Figure 1A-C**). URMC-099 pretreatment virtually abolished the IL-1β-induced increase in VCAM-1 IR ($p < 0.001$; **Figure 1A, C**). Additionally, it also reduced the basal IR of PECAM-1 by nearly half ($p = 0.001$; **Figure 1A, B**). We next characterized the effect of URMC-099 on the transcriptional response of bend.3 cells to IL-1β. In addition to *Vcam1*, we assayed the expression of *Spp1*, *Timp1*, and *Col1a1* — all of which are upregulated in activated BECs *in vivo* [19]. IL-1β upregulated *Vcam1* expression 59.16-fold ($p < 0.0001$) and elicited smaller (<2-fold) increases in *Spp1* ($p = 0.0002$) and *Timp1* ($p = 0.0004$) mRNA (**Figure 1D**). Of these genes, URMC-099 pretreatment significantly reduced *Vcam1* ($p < 0.0001$) and *Spp1* ($p = 0.0008$) mRNA levels (**Figure 1D**). In addition, IL-1β decreased the expression of *Col1a1* by 25% versus control ($p = 0.0077$), an effect that was not modulated by URMC-099

pretreatment (**Figure 1D**). Together, these experiments demonstrate that URMC-099 exerts anti-inflammatory effects on BEC activation *in vitro*.

URMC-099 prophylaxis inhibits cerebrovascular VCAM-1 IR after orthopedic surgery in CVN-AD mice

Based on our *in vitro* BEC results, we hypothesized that URMC-099 prophylaxis would inhibit cerebrovascular inflammation in the SLM of CVN-AD mice following surgery. Orthopedic surgery elicited a 1.7-fold increase in total VCAM-1 volume in the SLM relative to naïve, vehicle-treated controls (18542.5 ± 2318.7 um^3 *vs* WT 10840.8 ± 2825.2 um^3; $p < 0.0001$; **Figure 2A-D, E**). In agreement with our *in vitro* data, URMC-099 prophylaxis decreased total VCAM-1 in the SLM (12679.7 ± 1698.5 μm^3; $p = 0.0006$; **Figure 2E**). To determine whether these effects were specific to arterial or venous BECs, we used the arterial-specific dye Alexa 633 hydrazide [20] — which binds to elastin fibers present in arterioles — to distinguish between arterial and venous VCAM-1 objects in our analysis. Arterial VCAM-1 accounted for 27.3% of total VCAM-1 volume; further, there were no main effects of surgery [$F(1, 20) = 3.53$; $p = 0.08$] nor URMC-099 treatment [$F(1, 20) = 0.22$; $p = 0.65$] on arterial VCAM-1 levels (**Figure 2A'-D', E**). In contrast, we observed significant main effects of surgery [$F(1, 20) = 15.27$; $p = 0.0009$] and URMC-099 [$F(1, 20) = 14.32$; $p = 0.0012$] on venous VCAM-1 levels, mirroring the differences between groups observed in total VCAM-1 volume. To rule out a potential contribution of Aβ burden on cerebrovascular VCAM-1 levels, we visualized fibrillar Aβ in the SLM using the UV dye Amylo-Glo (**Figure 2A-D**). We did not detect significant differences in fibrillar Aβ between any experimental condition (**Figure 2F**), nor was there any correlation between fibrillar

Aβ levels and total VCAM-1 levels in the SLM (**Figure 2G**). Overall, these results indicate that URMC-099 has the greatest anti-inflammatory effect on venous VCAM-1 levels in the SLM. These data further suggest that therapeutic intervention earlier in the course of neuropathogenesis may elicit better outcomes in this DSD model. In support of this interpretation, pilot experiments in 12mos-old CVN mice demonstrated advanced pathology in hippocampal SLM with attenuated expression of VCAM-1 (*not shown*).

URMC-099 prophylaxis ameliorates synapse loss following orthopedic surgery in CVN-AD mice

Mouse models of PND and AD feature synaptic dysfunction and loss as pathological correlates of cognitive decline [21-23]. We hypothesized that the pre-existing neurodegenerative milieu present in CVN-AD mice would lower the threshold for synapse loss following a systemic inflammatory insult (i.e., orthopedic surgery) and that URMC-099 would protect synapses. To this end, we quantified synaptic punctae corresponding to pre- (Piccolo) and post-synaptic (Homer1, PSD95) elements in the SLM of mice 24 hours post-surgery (**Figure 3**). Surgery reduced Piccolo+ synaptic punctae by 33% ($p = 0.011$; **Figure 3A, C**), and Homer1+ and PSD95+ postsynaptic punctae by 10-14% ($p = 0.023$ and $p = 0.046$, respectively; **Figure 3A-B, D-E**) relative to naïve controls. URMC-099 pretreatment prevented loss of Piccolo+, PSD95+ and Homer1+ punctae comparable to control levels.

URMC-099 prophylaxis prevents the induction of MafB in microglia following orthopedic surgery in CVN-AD mice

Lineage-specific transcription factors have recently been shown to regulate pathological

microglial states under neurodegenerative and inflammatory conditions [24, 25]. In particular, the transcription factor MafB was shown recently to drive activation of spinal cord microglia in a mouse model of neuropathic pain [25]. Further, we have recently demonstrated that basal levels of MafB in microglial cells are dependent on availability of lipids in the extracellular milieu either from serum or from apoptotic debris of dying microglial cells [26]. Not only are apoptotic cells rich sources of lipids, so too are synapses [27]. Thus, we hypothesized that the neurodegenerative sequelae observed in our DSD model might also drive the upregulation of microglial MafB as a marker of microgliosis. To this end, we evaluated levels of the transcription factor MafB in SLM microglia following surgery and URMC-099 prophylaxis in CVN-AD mice. We visualized microglia using the pan-macrophage marker Iba1 and the microglia-specific marker Tmem119 [28]; only Iba1 cells co-labelled with Tmem119 were defined as microglia. Tmem119+ cells accounted for >95% of Iba1+ cells in our image set (**Supplemental Figure 1**). Orthopedic surgery increased the mean MafB IR per cell in SLM microglia ($p = 0.011$), an effect that was abrogated by URMC-099 prophylaxis ($p = 0.046$; **Figure 4A-C**). MafB induction in SLM microglia appeared homogenous in our frequency histogram analysis (**Figure 4C**). Overall, URMC-099 prevented the effect of surgery on microglial MafB induction. MafB is expressed in other CNS cell types, namely neurons [25, 29, 30]. To determine whether the induction of MafB was limited to microglia, we quantified the expression of non-microglial MafB IR (i.e., Iba1$^-$ MafB objects). We observed no main effects of surgery [$F(1, 20) = 0.9857$; $p = 0.3326$] nor URMC-099 treatment [$F(1, 20) = 1.266$; $p = 0.2738$] on non-microglial MafB IR (**Supplemental Figure 2**). These results indicate the microglial MafB, but not neuronal MafB, is increased following orthopedic surgery in CVN-AD mice.

Orthopedic surgery and URMC-099 does not affect C1q deposition and microglial CD68/Iba1 immunoreactivity in CVN-AD mice

The opsonin C1q mediates microglia-dependent synapse loss in diverse contexts [22, 31] and is transcriptionally regulated by MafB [32]. These observations raise the possibility that microglia eliminate synapses *via* increased C1q deposition following orthopedic surgery. Although C1q expression was very robust throughout the SLM (**Figure 5A**), in agreement with previous findings by Stephan et al. [33] we observed no effects of surgery [$F(1, 20) = 0.4938$; $p = 0.4903$] nor URMC- 099 treatment [$F(1, 20) = 0.0280$; $p = 0.8689$] on C1q deposition (**Figure 5B**). We next quantified the lysosomal marker CD68, whose expression is associated with activated phagocytic microglia [34] in Iba1+ cells in the SLM. However, these cells in the SLM contained high levels of CD68 regardless of condition; but neither orthopedic surgery [$F(1, 20) = 0.8440$; $p = 0.3692$] nor URMC-099 treatment [$F(1, 20) = 0.8440$; $p = 3692$] altered CD68 levels in Iba1+ cells (**Figure 5C**). We then quantified changes in microglia activation utilizing the pan-myeloid marker, Iba1. Although not well understood, during microgliosis expression of Iba1 is increased along with a thickening of processes. After surgery we found there is a positive trend of Iba1 expression along with a negative trend in surface area compared to sham ($P = 0.0511$ and $P = 0.0921$, respectively; **Figure 5C-D**). Taken together, these results demonstrate that C1q, in contrast to its roles during brain development and models of AD [22, 31], does not participate in microglial phagocytosis of synapses in this orthopedic model of DSD.

Based on our results in this model of DSD, we have summarized URMC-099's

different sites of action in a visual abstract (**Figure 6**). Overall, URMC-099 pretreatment prior to surgery exerts therapeutic effects *via* inhibition of several kinase pathways in multiple vascular, immune and neuronal cell types that include preventing potential VCAM-1-mediated effects, which we hypothesize results in increased transcellular passage of inflammatory leukocytes in post-capillary venules in the SLM, deactivation of the microglial transcription factor MafB, and rescue of vulnerable pre- and postsynaptic elements in the SLM.

Discussion

Here, we show that URMC-099 prophylaxis is effective in the CVN-AD mouse model of DSD *prior* to the onset of age-dependent progressive vascular injury by mitigating brain endothelial cell activation (i.e., VCAM-1 upregulation) and synapse loss. The correlation of these events with the induction of microglial MafB immunoreactivity suggests, but does not prove, a role for microglia in mediating the effects of systemic inflammation (i.e., orthopedic surgery) on synaptic integrity in these mice. Our findings are consistent with the model proposed by Yousef et al. (2019) [11] to explain the deleterious effects of aged plasma on microglia. In fact, this model posits pro-inflammatory cytokines present in the systemic milieu of aged mice (e.g., TNF-α and IL-1β) — the same ones induced systemically in our orthopedic surgery model [35, 36] — upregulate VCAM-1 on BECs, leading to sustained inflammatory activity at the BBB interface and transmission of inflammatory signals from the inflamed endothelium to microglia [11] and by extension, microglial phagocytosis of hippocampal synapses. We contend that URMC-099 exerts at least some of its therapeutic effects by inhibiting

vascular signaling through VCAM-1 (i.e., BEC) that would otherwise initiate the inflammatory cascade that leads to microgliosis and synaptic loss.

Indeed, systemic factors induce changes in microglial reactivity by multiple mechanisms. BECs relay systemic inflammatory signals to microglia *via* soluble factors [37, 38] and direct microglial contacts with BECs [39-42]. In addition, breakdown of BEC tight junctions permits the direct entry of systemic factors (e.g., fibrinogen, systemic complement protein, etc.), many of which profoundly affect microglial function [43, 44]. Finally, peripheral leukocytes can infiltrate the CNS and release inflammatory factors to nearby cells. Indeed, CCR2+ monocytes infiltrate the hippocampal parenchyma *via* the choroid plexus following orthopedic surgery in mice [45, 46]. In the present study, the vast majority (>95%) of SLM Iba1+ cells also expressed the microglia-specific marker Tmem119 [47], indicating that they were not peripherally derived. We believe the Tmem119-negative cells were either perivascular macrophages, which lack Tmem119 expression [48], or reactive microglia that have down-regulated their expression of this marker [49]. However, the selective increase of VCAM-1 on post-capillary venules, through which leukocytes preferentially transmigrate [50], supports the possibility of increased tethering of leukocytes to the endothelium and infiltration in the SLM following orthopedic surgery, although such infiltration may be limited to the perivascular space rather than the CNS parenchyma.

Pathologic cascade of signaling events after surgery are depicted in **Figure 6.** These include inflammatory events that involve vascular endothelium, microglia and synaptic compartments in the hippocampal SLM. These events share striking similarities to dysregulated innate immune effector cells in peripheral hepatic inflammation.

Specifically, in previous work using a dietary model of nonalcoholic steatohepatitis (NASH) that induces hepatotoxic lipoapoptosis and inflammation [51], chronic dosing with URMC-099 decreased the expression of "inflammatory" transcripts *Timp1*, *Col1α1*, and *Spp1* in whole liver extracts [51]. In the present study, we examined the expression of these genes in a brain endothelial cell line (bend.3) to determine the extent of overlap between liver and the BBB in inflammatory signaling cascades that affect vascular endothelium [19]. Pro-inflammatory IL-1β stimulation upregulated *Timp1* and *Spp1*, but not *Col1α1*, in bend.3 cells; further, URMC-099 prevented the induction of *Spp1* in these cells (**Figure 1**). The induction of these genes in diverse inflammatory contexts (i.e. DSD and NASH), combined with the conservation of signaling pathways upstream of these effects, further supports a broad-spectrum mechanism for URMC-099 in multiple end-organs and cell types such as the hippocampal SLM in response to neuroinflammation (**Figure 6**). Finally, it is worth noting that NASH may also contribute to the neuropathogenesis of AD via metabolic modification of Aβ [52] while pathologic changes in amyloid precursor protein processing may contribute to NASH [53].

Although the function of microglial MafB in the present study is unclear, several pathological features were shown to mediate disease progression in atherosclerotic mice and therefore provide an interesting comparison for speculation. Atherosclerotic lesions form *via* a VCAM-1-dependent process where vascular inflammation induces monocyte extravasation into the perivascular space [54]. These extravasated monocytes subsequently scavenge highly oxidized low-density lipoprotein (oxLDL) and convert into foam cells with induction of MafB in an LXR-dependent pathway [54-56]. Interestingly, induction of MafB in foam cells inhibits their apoptosis *via* upregulation of apoptosis

inhibitor of macrophages, leading to stabilization of atherosclerotic plaques [55, 56]. In our model, orthopedic surgery induced upregulation of VCAM-1 in SLM post-capillary venules (**Figure 2**), loss of synaptic elements (**Figure 3**), and increased MafB immunoreactivity in SLM microglia (**Figure 4**). Substrates that may drive induction of MafB following surgery are not well characterized. Both oxidative stress [57] and engulfment of apoptotic cells [32] have been shown to induce MafB expression in macrophages. Because efferocytosis is dependent on LXR [58], it is conceivable that orthopedic surgery, when combined with pre-existing neurodegeneration (i.e., AD pathology), causes microglial engulfment of focal apoptotic synapses (i.e., synaptosis) and other cellular debris [59], leading to MafB induction. Future work is necessary to prove this, although a recent report showing microglial induction of MafB following peripheral nerve injury supports this hypothesis [25].

Microglia pathologically interact with synaptic elements in mouse models of neurodegeneration and neuroinflammation [14, 15, 22, 40, 60]. Because microglia mediate synapse loss in mouse models of AD *via* complement-dependent pruning processes [22], and tibial fracture/fixation upregulated MafB, which in turn transcriptionally regulates C1q [32], we investigated whether synapse loss in our DSD model might also depend on C1q. Here we did not observe changes in C1q deposition or microglial CD68 immunoreactivity following orthopedic surgery in CVN-AD mice (**Figure 5**). It is worth noting, however, that C1q is deposited at high levels in the SLM of wild-type [33] and CVN-AD mice (this study). Moreover, we observed high levels of CD68 selectively in SLM microglia compared to surrounding regions across all our conditions. Thus, these two factors may predispose the SLM of CVN-AD mice to synaptic loss

following systemic and/or CNS inflammation. Finally, we cannot completely exclude the possibility that our synaptic data reflects changes in the expression of genes encoding Piccolo, PSD95, and Homer1, as has been observed in AD patients [61], or the clustering of these proteins in synaptic structures (that would influence their ability to form punctae). Even so, changes in synaptic gene expression correlate with cognitive impairment in AD patients [62, 63], and microglial depletion ameliorates pathological changes in synaptic gene expression in mouse AD models [64]. Taken together, we believe the amelioration of synaptic loss we observed in our model of DSD is likely microglial-dependent and these are tractable targets for URMC-099 prophylaxis in protecting the neurovascular unit from postoperative complications including delirium and dementia.

Conclusions

Using our orthopedic model of tibial fracture/fixation in six-month-old CVN mice, we have demonstrated that damage to the BBB resulting in endothelial activation with increased expression of VCAM-1 in post-capillary venules of hippocampal SLM, associated microgliosis and damage to synaptic architecture, can be prevented with prophylactic administration of the MLK3/LRRK2 broad-spectrum inhibitor, URMC-099. Based on these findings, we conclude that this therapeutic approach may represent an intervention to significantly decrease deleterious effects of DSD in the elderly population at risk for morbidity and mortality after surgery.

Declarations

All manuscripts must contain the following sections under the heading 'Declarations':

- Ethics approval: The procedures followed to provide tissues from APPSwDI/mNos2$^{-/-}$ (CVN-AD) mice were performed in strict compliance with animal protocols approved by the Institutional Animal Care and Use Committees (IACUC) of Duke University (A249-17-11).
- Consent for publication: All authors have reviewed the data and its interpretation and consent to the submission of this publication.
- Availability of data and material: All data generated or analyzed during this study are included in this published article and its supplementary information files.
- Competing interests: Niccolò Terrando is on the scientific advisory board of Pioneura Corp.; Harris A Gelbard is the chief science officer of Pioneura Corp. Pioneura Corp. holds the exclusive license for the development of URMC-099, but contributed no funding for this work.
- Funding: NIA R01AG057525 (NT)
- Authors' contributions: PMR performed the experiments, analyzed the data and wrote and edited the manuscript. HL analyzed the data, wrote and edited the manuscript. RV performed experiments on CVN-AD mice. NT and HAG. supervised PMR and HL and contributed to the interpretation of the data.
- Acknowledgements: We thank Angela Stout in the Gelbard lab for her technical expertise.
- Authors' information (optional). See front page

Figure legends

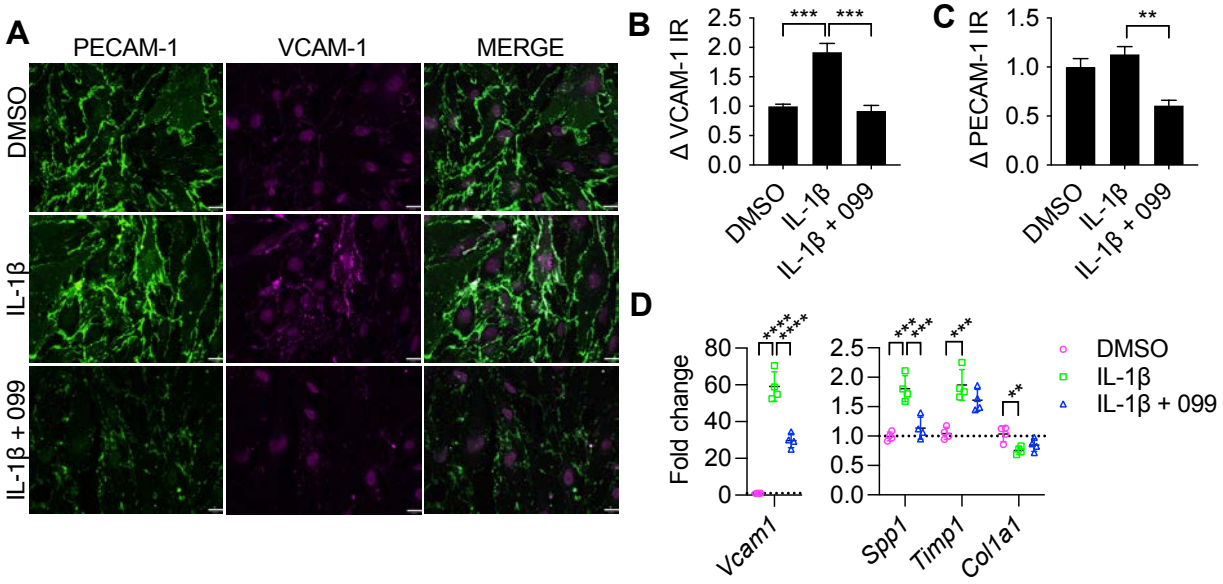

Figure 1. URMC-099 inhibits BEC activation *in vitro*. Serum-deprived Bend.3 cells were pre-treated with URMC-099 (099) or DMSO for 30 min, after which cells were stimulated with IL-1β (10 ng/mL). (A) Representative images of VCAM-1 and PECAM-1 staining in bend.3 cells; scale bar = 15 μm. (B) Quantification of PECAM-1 IR, represented as fold change. (C) Quantification of VCAM-1 IR, represented as fold change. (D) qPCR analysis of bend.3 transcriptional response to IL-1B and URMC-099 treatment. Values presented as mean ± SEM (N = 4 cell culture wells). ** $P < 0.01$, *** $P < 0.001$, **** $P < 0.0001$ for indicated comparisons; one-way ANOVA with Dunnett's multiple comparison test (B-D).

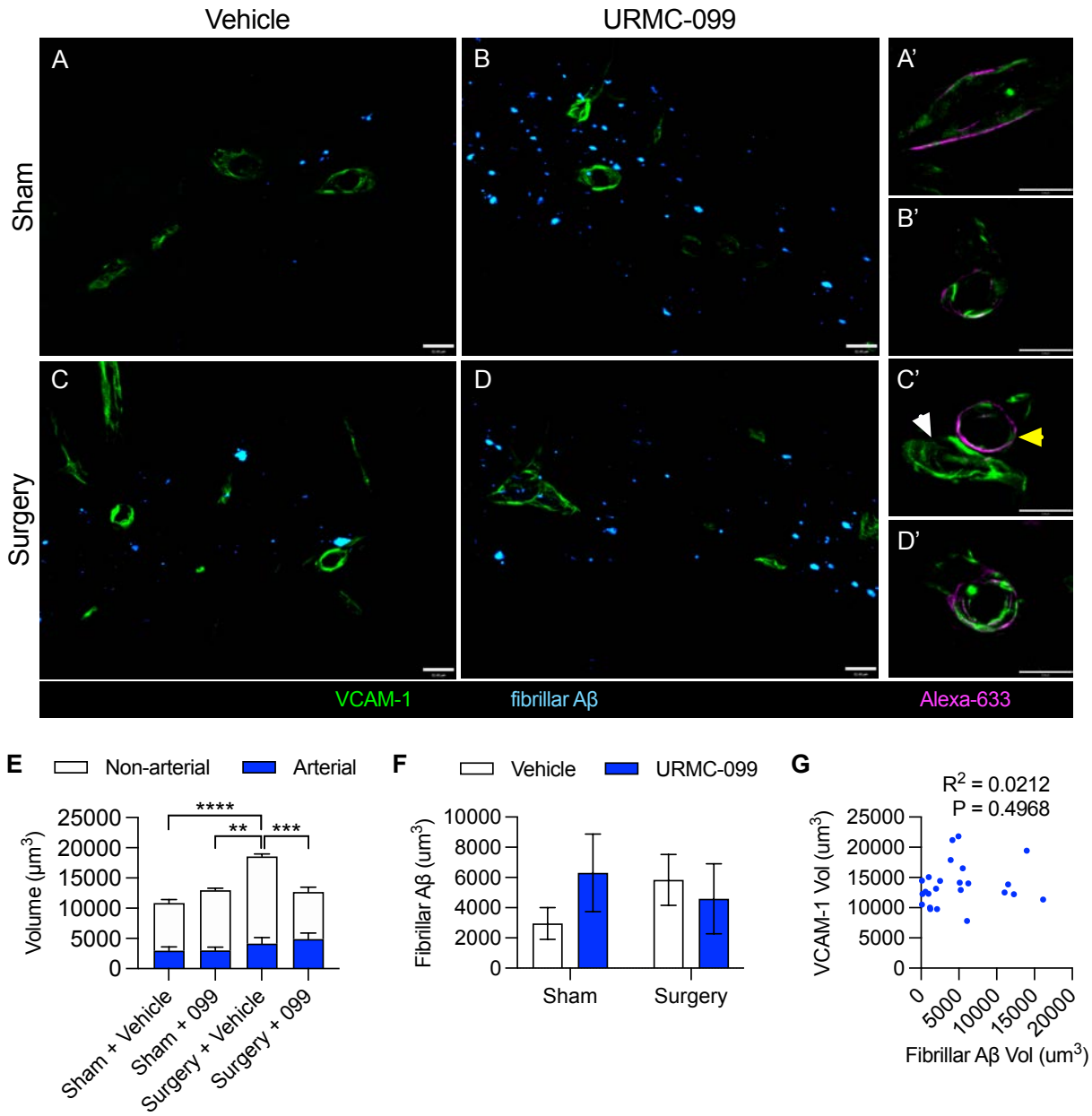

Figure 2. URMC-099 prophylaxis prevents the induction of VCAM-1 in the SLM of CVN-AD mice following surgery. Six-month-old CVN-AD mice (N=6/group) received three doses i.p. of URMC-099 (10 mg/kg) prior to undergoing sham or orthopedic surgery. Brains were harvested 24 h post-surgery for IHC. (A-D) Representative images depicting VCAM-1 (green) and fibrillar AB (cyan). (A'-D') Representative images depicting arterial VCAM-1 vessels using the artery-specific dye Alexa 633-hydrazide (magenta); images correspond to experimental conditions represented

by A-D; scale bar = 32μm. (E) Quantification of total VCAM-1 volume (full bars), venous VCAM-1 volume (white bars), and arterial VCAM-1 volume (blue bars); statistical comparisons are shown for total VCAM-1. (F) Quantification of fibrillar AB. (G) Correlation between total VCAM-1 volume and fibrillar AB volume. Values presented as mean ± SEM (N = 6); ** $P < 0.01$, *** $P < 0.001$, **** $P < 0.0001$ for indicated comparisons; two-way ANOVA with Holm-Sidak's multiple comparison test (E, F) or Pearson's coefficient (D).

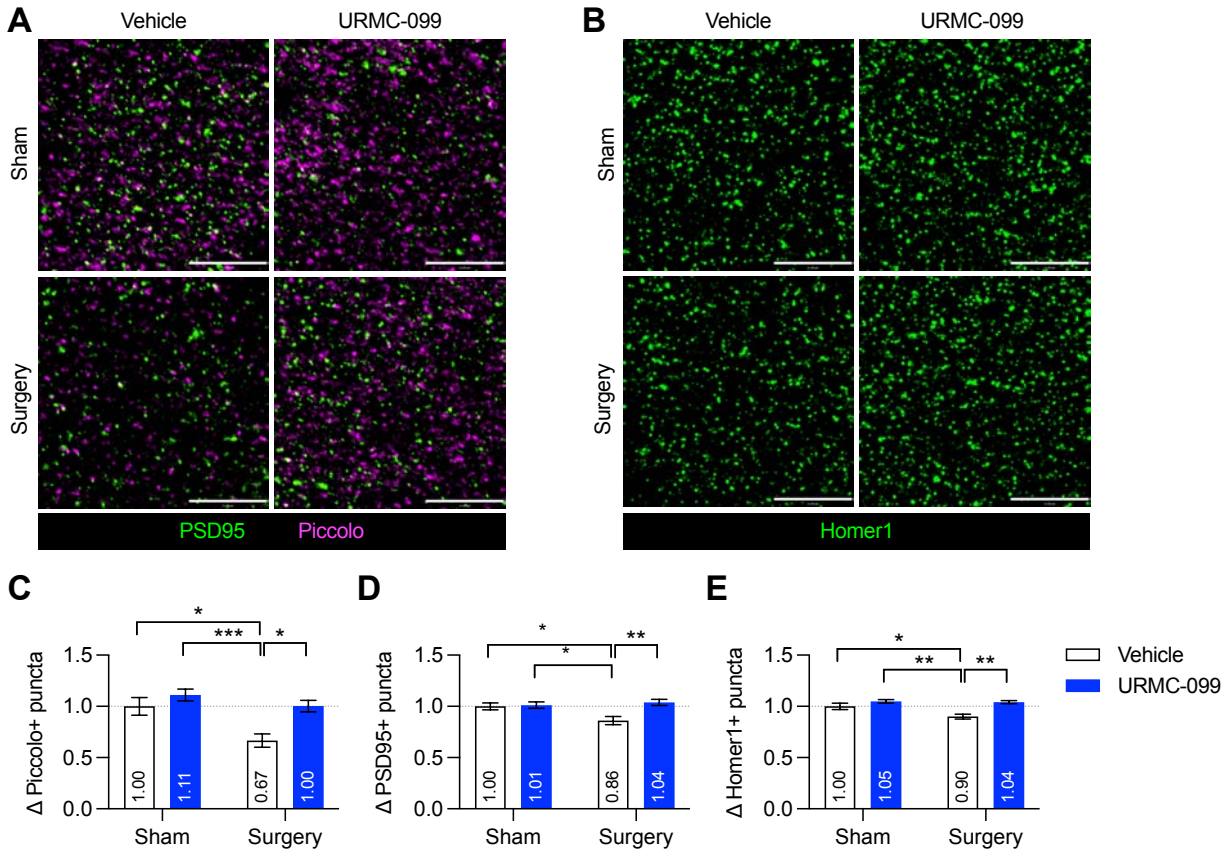

Figure 3. URMC-099 prevents synapse loss in the SLM of CVN-AD mice following orthopedic surgery. Six-month-old CVN-AD mice (N=6/group) received three doses i.p. of URMC-099 (10 mg/kg) prior to undergoing sham or orthopedic surgery. Brains were harvested 24 h post-surgery for IHC. (A) Representative ROIs depicting PSD95+ (postsynaptic) and Piccolo+ (presynaptic) puncta; scale bar = 11 μm. (B) Representative ROIs depicting Homer1+ (postsynaptic) puncta; scale bar = 11 μm. (C) Quantification of presynaptic Piccolo+ puncta, represented as fold change. (D) Quantification of postsynaptic PSD95+ puncta, represented as fold change. (E) Quantification of postsynaptic Homer1+ puncta, represented as fold change. Values presented as mean ± SEM (N = 6); * $P < 0.05$, ** $P < 0.01$, *** $P < 0.001$ for indicated comparisons; two-way ANOVA with Holm-Sidak's multiple comparison test (C-E).

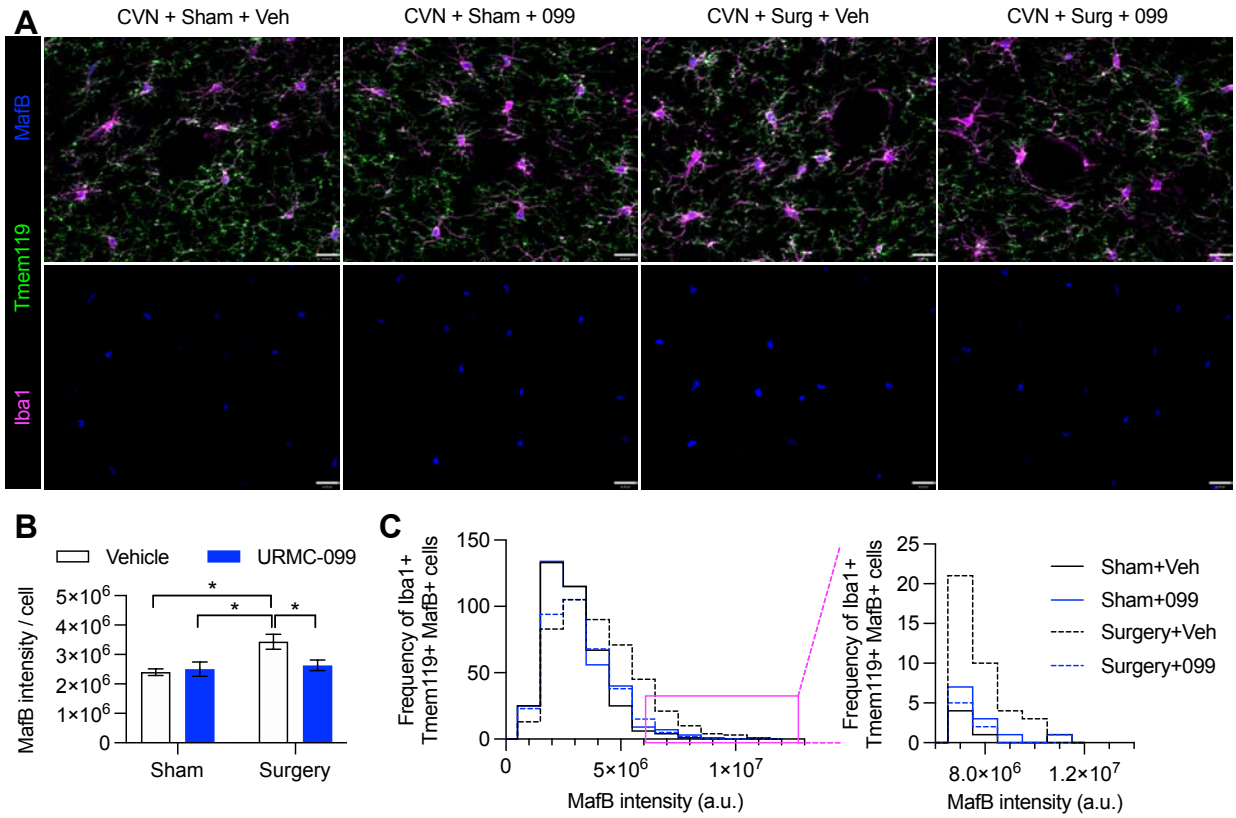

Figure 4. URMC-099 prevents changes in MafB microglial expression in the SLM of CVN-AD mice following orthopedic surgery. Six-month-old CVN-AD mice (N=6/group) received three doses i.p. of URMC-099 (10 mg/kg) prior to undergoing sham or orthopedic surgery. Brains were harvested 24 h post-surgery for IHC. (A) Representative images depicting the pan-macrophage marker Iba1 (magenta), the microglia-specific marker Tmem119 (green), and the transcription factor MafB (blue); scale bar = 16 μm. (B) Quantification of mean MafB intensity per microglia. (C) Frequency histogram showing the number of microglia per MafB intensity bin (bin size = 1.0×10^6 a. u.). (C, inset) Frequency histogram depicting cell frequencies with high MafB intensity. Values presented as mean ± SEM (N = 6); * $P < 0.05$ for indicated comparisons; two-way ANOVA with Holm-Sidak's multiple comparison test (B, E).

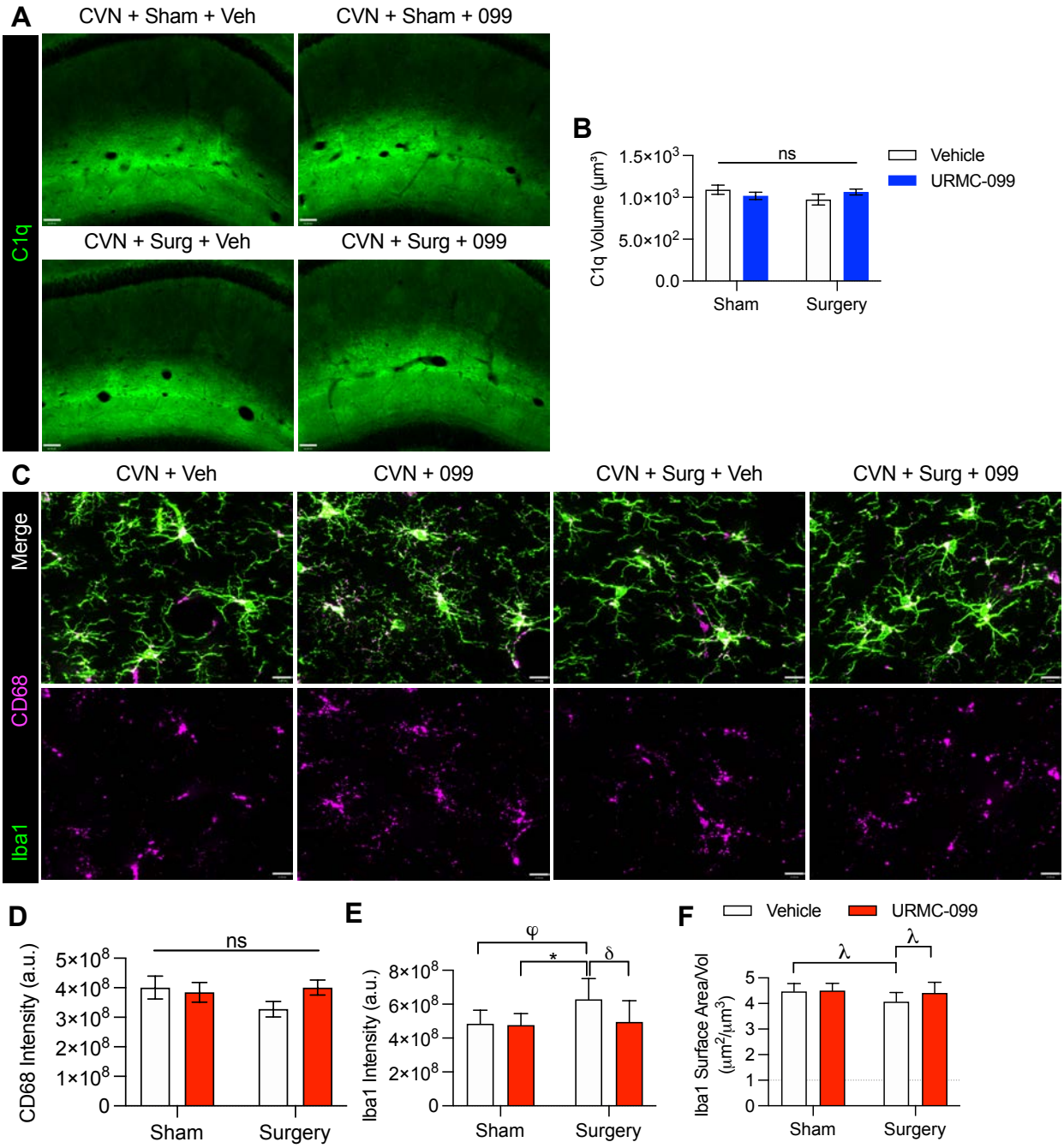

Figure 5. URMC-099 pretreatment does not change C1q or CD68 expression levels after surgery in the SLM of CVN-AD mice following orthopedic surgery. Six-month-old CVN-AD mice (N=6/group) received three doses i.p. of URMC-099 (10 mg/kg) prior to undergoing sham or orthopedic surgery. (A) Representative image of C1q (green) localizing in the SLM; scale bar = 60µm. (B) Quantification of C1q volume in the SLM. (C) Representative images depicting the pan-

macrophage marker Iba1 (green), the lysosomal marker CD68 (magenta); scale bar = 11 μm. No effects were observed on CD68 expression (D), but surgery increased Iba-1 expression and decreased surface area with a trend in URMC-099-mediated decreases (E, F). Values presented as mean ± SEM (N = 6); * $p < 0.05$; φ $p = 0.0511$; δ $p = 0.0636$; λ $p = 0.0921$ for indicated comparisons; two-way ANOVA with Holm-Sidak's multiple comparison test (B-D).

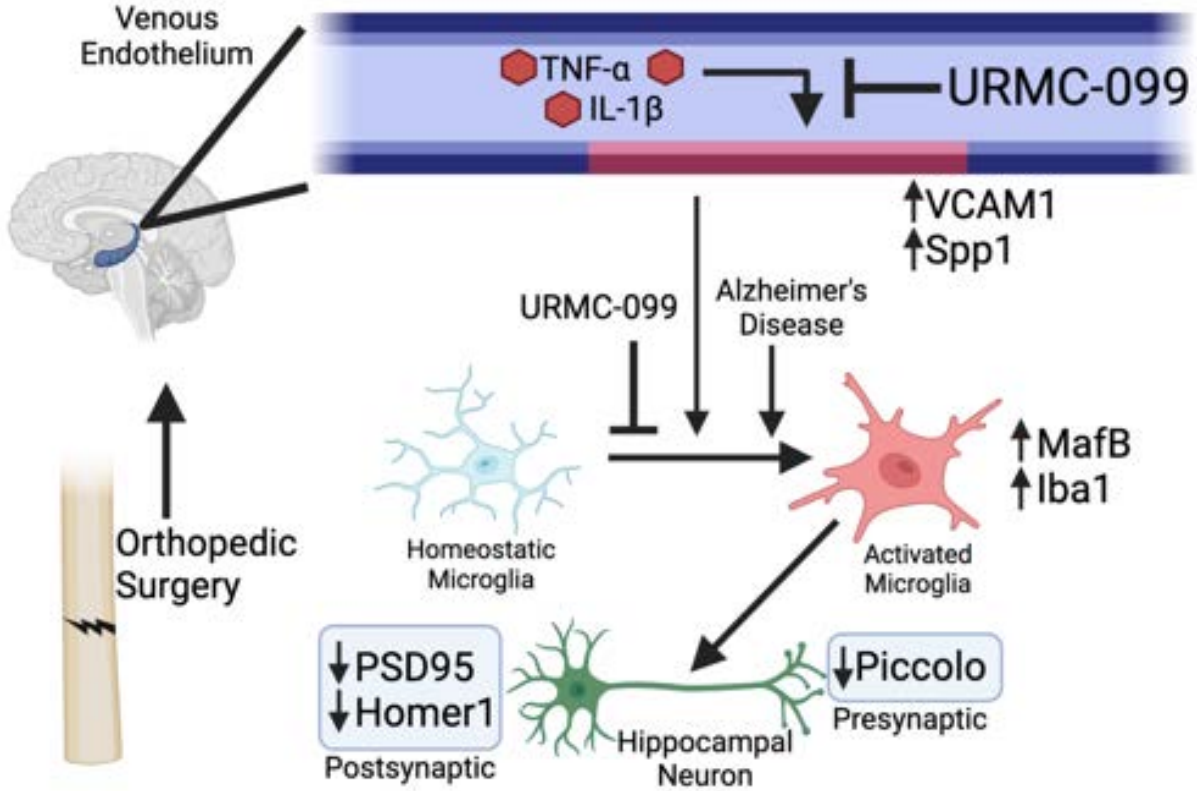

Figure 6. Proposed relationships between URMC-099 pretreatment and changes in endothelial, microglial and synaptic markers following surgery in six-month-old CVN-AD mice.

Supplementary figures

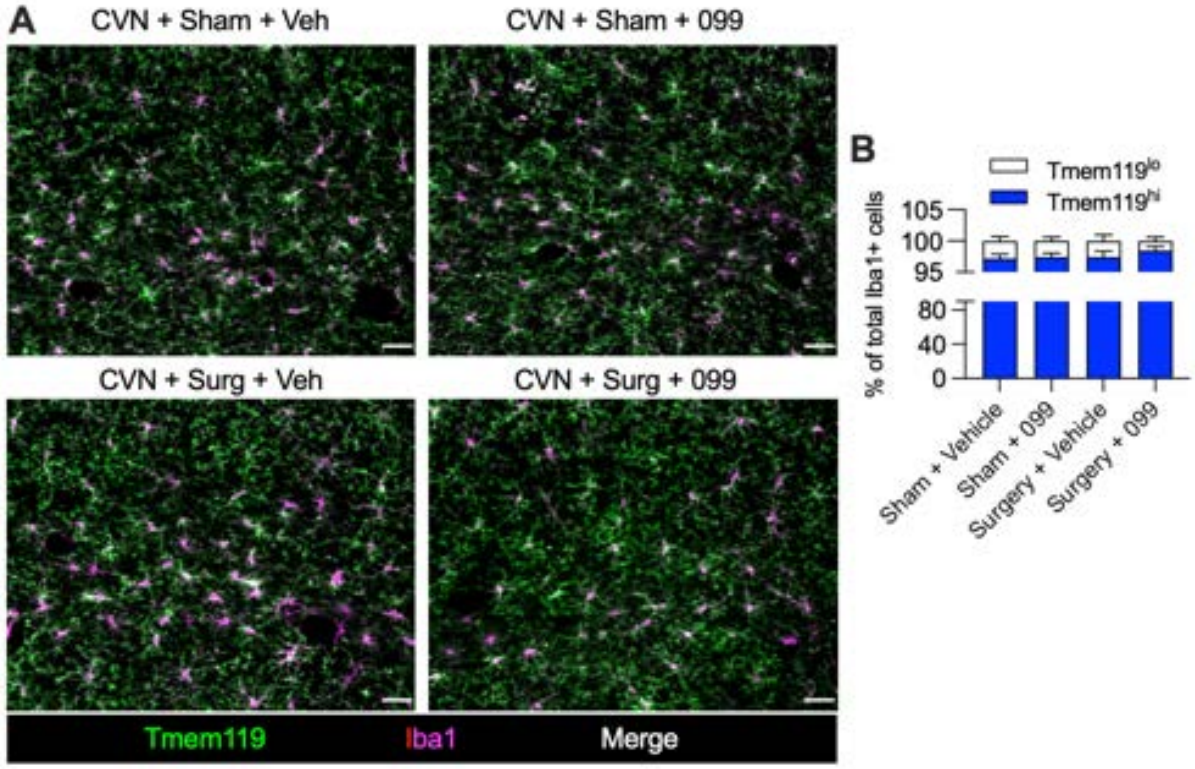

Supplement Figure 1. Iba1+ cells in the SLM are predominantly microglia. Six- month-old CVN mice (N=6/group) received three doses i.p. of URMC-099 (10 mg/kg) prior to undergoing sham or orthopedic surgery. Brains were harvested 24 h post-surgery for IHC. (A) Quantification of Tmem119^{hi} and Tmem119^{lo} Iba1+ cells in the SLM for surgical and URMC-099 treatment groups. (B) Quantification of mean Tmem119^{hi} and Tmem119^{lo} cell numbers per 40X field of view. Values presented as mean ± SEM (n = 6); two-way ANOVA with Holm-Sidak's multiple comparison test (B).

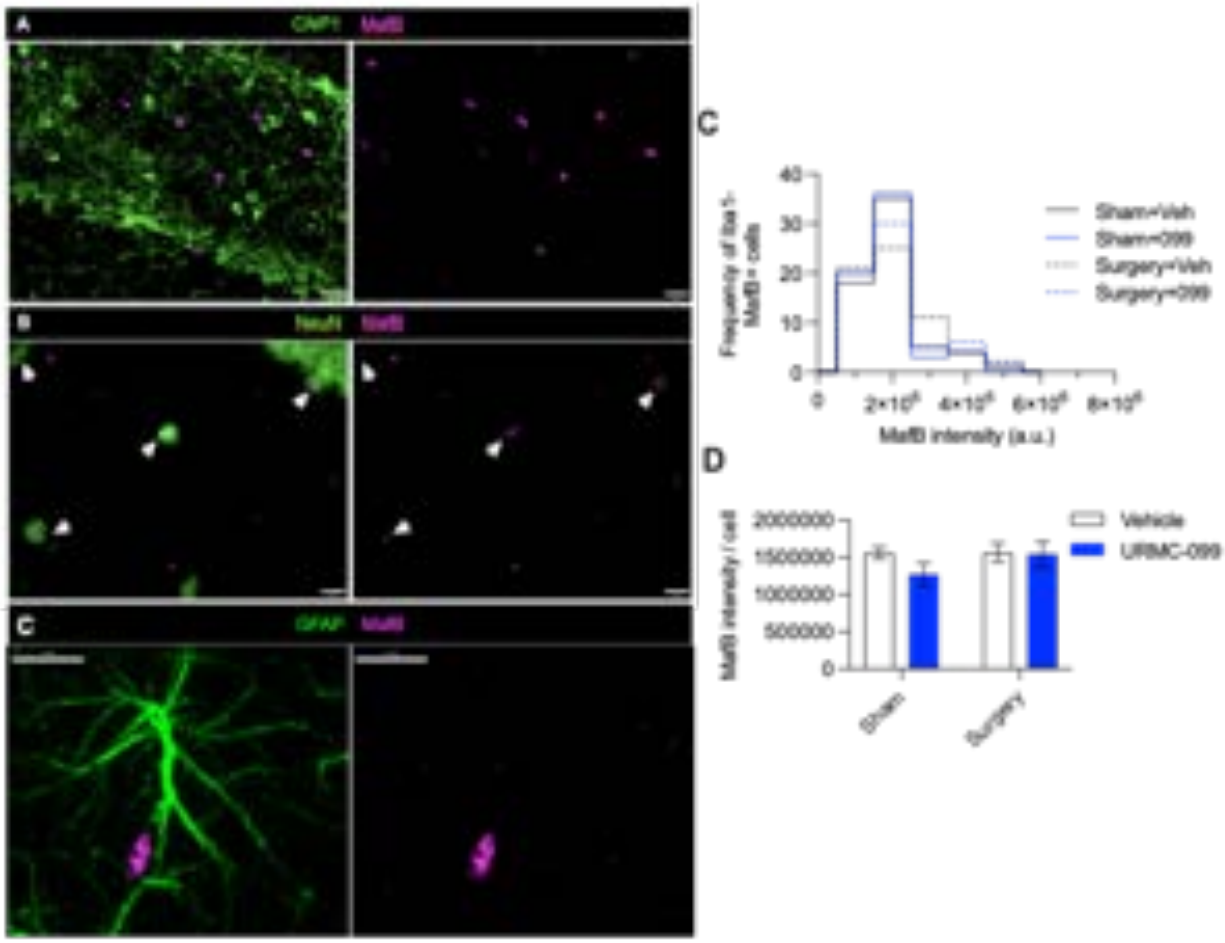

Supplement Figure 2. Orthopedic surgery and URMC-099 treatment had no effect on non-microglial MafB immunoreactivity in the SLM. Six-month-old CVN-AD mice (N=6/group) received three doses i.p. of URMC-099 (10 mg/kg) prior to undergoing sham or orthopedic surgery. Brains were harvested 24 h post-surgery for IHC. Representative image of MafB (magenta) co-labeling oligodendrocyte-specific marker (CNP1, green), neuronal-specific marker (NeuN, green), and astrocyte-specific marker (GFAP, green) (A, B, and C respectively); scale bar = 16 μm (A, B) 11 μm (C). (D) Frequency histogram showing the number of microglia per MafB intensity bin (bin size = 1.0×10^6 a. u.). (D) Quantification of mean MafB intensity normalized to the number of $Iba1^-$ $MafB^+$ nuclei. Values presented as mean ± SEM (n = 6); two-way ANOVA with Holm-Sidak's multiple comparison test (D).

References

1. Elie, M., et al., *Delirium risk factors in elderly hospitalized patients.* J Gen Intern Med, 1998. **13**(3): p. 204-12.
2. Lee, H.B., et al., *Impact of Delirium After Hip Fracture Surgery on One-Year Mortality in Patients With or Without Dementia: A Case of Effect Modification.* Am J Geriatr Psychiatry, 2017. **25**(3): p. 308-315.
3. Wilson, J.E., et al., *Delirium.* Nat Rev Dis Primers, 2020. **6**(1): p. 90.
4. Fong, T.G., et al., *The interface between delirium and dementia in elderly adults.* Lancet Neurol, 2015. **14**(8): p. 823-832.
5. Davis, D.H., et al., *Delirium is a strong risk factor for dementia in the oldest-old: a population-based cohort study.* Brain, 2012. **135**(Pt 9): p. 2809-16.
6. Wang, P., et al., *Neurovascular and immune mechanisms that regulate postoperative delirium superimposed on dementia.* Alzheimers Dement, 2020. **16**(5): p. 734-749.
7. Kan, M.J., et al., *Arginine deprivation and immune suppression in a mouse model of Alzheimer's disease.* J Neurosci, 2015. **35**(15): p. 5969-82.
8. Hoos, M.D., et al., *Longitudinal study of differential protein expression in an Alzheimer's mouse model lacking inducible nitric oxide synthase.* J Proteome Res, 2013. **12**(10): p. 4462-77.
9. Colton, C.A., et al., *mNos2 deletion and human NOS2 replacement in Alzheimer disease models.* J Neuropathol Exp Neurol, 2014. **73**(8): p. 752-69.
10. Wilcock, D.M., et al., *Progression of amyloid pathology to Alzheimer's disease pathology in an amyloid precursor protein transgenic mouse model by removal of nitric oxide synthase 2.* J Neurosci, 2008. **28**(7): p. 1537-45.
11. Yousef, H., et al., *Aged blood impairs hippocampal neural precursor activity and activates microglia via brain endothelial cell VCAM1.* Nat Med, 2019. **25**(6): p. 988-1000.
12. Montagne, A., et al., *Blood-brain barrier breakdown in the aging human hippocampus.* Neuron, 2015. **85**(2): p. 296-302.
13. Yang, X., et al., *A novel mechanism of memory loss in Alzheimer's disease mice via the degeneration of entorhinal-CA1 synapses.* Mol Psychiatry, 2018. **23**(2): p. 199-210.
14. Marker, D.F., et al., *The new small-molecule mixed-lineage kinase 3 inhibitor URMC-099 is neuroprotective and anti-inflammatory in models of human immunodeficiency virus-associated neurocognitive disorders.* J Neurosci, 2013. **33**(24): p. 9998-10010.
15. Bellizzi, M.J., et al., *The Mixed-Lineage Kinase Inhibitor URMC-099 Protects Hippocampal Synapses in Experimental Autoimmune Encephalomyelitis.* eNeuro, 2018. **5**(6).
16. Miller-Rhodes, P., et al., *The broad spectrum mixed-lineage kinase 3 inhibitor URMC-099 prevents acute microgliosis and cognitive decline in a mouse model of perioperative neurocognitive disorders.* J Neuroinflammation, 2019. **16**(1): p. 193.
17. Montesano, R., et al., *Increased proteolytic activity is responsible for the aberrant morphogenetic behavior of endothelial cells expressing the middle T oncogene.* Cell, 1990. **62**(3): p. 435-45.
18. Glynn, M.W. and A.K. McAllister, *Immunocytochemistry and quantification of protein colocalization in cultured neurons.* Nat Protoc, 2006. **1**(3): p. 1287-96.
19. Munji, R.N., et al., *Profiling the mouse brain endothelial transcriptome in health and disease models reveals a core blood-brain barrier dysfunction module.* Nat Neurosci, 2019. **22**(11): p. 1892-1902.
20. Shen, Z., et al., *An artery-specific fluorescent dye for studying neurovascular coupling.* Nat Methods, 2012. **9**(3): p. 273-6.
21. Terrando, N., et al., *Aspirin-triggered resolvin D1 prevents surgery-induced cognitive decline.* FASEB J, 2013. **27**(9): p. 3564-71.

22. Hong, S., et al., *Complement and microglia mediate early synapse loss in Alzheimer mouse models.* Science, 2016. **352**(6286): p. 712-716.
23. Femenia, T., et al., *Disrupted Neuroglial Metabolic Coupling after Peripheral Surgery.* J Neurosci, 2018. **38**(2): p. 452-464.
24. Crotti, A., et al., *Mutant Huntingtin promotes autonomous microglia activation via myeloid lineage-determining factors.* Nat Neurosci, 2014. **17**(4): p. 513-21.
25. Tozaki-Saitoh, H., et al., *Transcription factor MafB contributes to the activation of spinal microglia underlying neuropathic pain development.* Glia, 2019. **67**(4): p. 729-740.
26. Miller-Rhodes, P. and H.A. Gelbard, *The Cell Culture Environment Regulates the Transcription Factor MafB in BV-2 Microglia.* Matters (Zur), 2021. **2021**.
27. Pfrieger, F.W., *Role of cholesterol in synapse formation and function.* Biochim Biophys Acta, 2003. **1610**(2): p. 271-80.
28. Bennett, M.L., et al., *New tools for studying microglia in the mouse and human CNS.* Proc Natl Acad Sci U S A, 2016. **113**(12): p. E1738-46.
29. Yu, W.M., et al., *A Gata3-Mafb transcriptional network directs post-synaptic differentiation in synapses specialized for hearing.* Elife, 2013. **2**: p. e01341.
30. Pai, E.L., et al., *Mafb and c-Maf Have Prenatal Compensatory and Postnatal Antagonistic Roles in Cortical Interneuron Fate and Function.* Cell Rep, 2019. **26**(5): p. 1157-1173.e5.
31. Bialas, A.R. and B. Stevens, *TGF-β signaling regulates neuronal C1q expression and developmental synaptic refinement.* Nat Neurosci, 2013. **16**(12): p. 1773-82.
32. Tran, M.T.N., et al., *MafB is a critical regulator of complement component C1q.* Nat Commun, 2017. **8**(1): p. 1700.
33. Stephan, A.H., et al., *A dramatic increase of C1q protein in the CNS during normal aging.* J Neurosci, 2013. **33**(33): p. 13460-74.
34. Hendrickx, D.A.E., et al., *Staining of HLA-DR, Iba1 and CD68 in human microglia reveals partially overlapping expression depending on cellular morphology and pathology.* J Neuroimmunol, 2017. **309**: p. 12-22.
35. Cibelli, M., et al., *Role of interleukin-1beta in postoperative cognitive dysfunction.* Ann Neurol, 2010. **68**(3): p. 360-8.
36. Terrando, N., et al., *Tumor necrosis factor-alpha triggers a cytokine cascade yielding postoperative cognitive decline.* Proc Natl Acad Sci U S A, 2010. **107**(47): p. 20518-22.
37. Liu, X., et al., *Cell-Type-Specific Interleukin 1 Receptor 1 Signaling in the Brain Regulates Distinct Neuroimmune Activities.* Immunity, 2019. **50**(2): p. 317-333.e6.
38. Zhu, L., et al., *Interleukin-1 causes CNS inflammatory cytokine expression via endothelia-microglia bi-cellular signaling.* Brain Behav Immun, 2019. **81**: p. 292-304.
39. Lassmann, H., et al., *Microglial cells are a component of the perivascular glia limitans.* J Neurosci Res, 1991. **28**(2): p. 236-43.
40. Bisht, K., et al., *Dark microglia: A new phenotype predominantly associated with pathological states.* Glia, 2016. **64**(5): p. 826-39.
41. Lou, N., et al., *Purinergic receptor P2RY12-dependent microglial closure of the injured blood-brain barrier.* Proc Natl Acad Sci U S A, 2016. **113**(4): p. 1074-9.
42. Joost, E., et al., *Microglia contribute to the glia limitans around arteries, capillaries and veins under physiological conditions, in a model of neuroinflammation and in human brain tissue.* Brain Struct Funct, 2019. **224**(3): p. 1301-1314.
43. Bohlen, C.J., et al., *Diverse Requirements for Microglial Survival, Specification, and Function Revealed by Defined-Medium Cultures.* Neuron, 2017. **94**(4): p. 759-773.e8.
44. Merlini, M., et al., *Fibrinogen Induces Microglia-Mediated Spine Elimination and Cognitive Impairment in an Alzheimer's Disease Model.* Neuron, 2019. **101**(6): p. 1099-1108.e6.
45. Terrando, N., et al., *Resolving postoperative neuroinflammation and cognitive decline.*

Ann Neurol, 2011. **70**(6): p. 986-995.
46. Feng, X., et al., *Microglia mediate postoperative hippocampal inflammation and cognitive decline in mice.* JCI Insight, 2017. **2**(7): p. e91229.
47. Bennett, F.C., et al., *A Combination of Ontogeny and CNS Environment Establishes Microglial Identity.* Neuron, 2018. **98**(6): p. 1170-1183.e8.
48. Goldmann, T., et al., *Origin, fate and dynamics of macrophages at central nervous system interfaces.* Nat Immunol, 2016. **17**(7): p. 797-805.
49. Krasemann, S., et al., *The TREM2-APOE Pathway Drives the Transcriptional Phenotype of Dysfunctional Microglia in Neurodegenerative Diseases.* Immunity, 2017. **47**(3): p. 566-581.e9.
50. Owens, T., I. Bechmann, and B. Engelhardt, *Perivascular spaces and the two steps to neuroinflammation.* J Neuropathol Exp Neurol, 2008. **67**(12): p. 1113-21.
51. Tomita, K., et al., *Mixed-lineage kinase 3 pharmacological inhibition attenuates murine nonalcoholic steatohepatitis.* JCI Insight, 2017. **2**(15).
52. Hefner, M., et al., *Cardiometabolic Modification of Amyloid Beta in Alzheimer's Disease Pathology.* Front Aging Neurosci, 2021. **13**: p. 721858.
53. Guo, Y., et al., *Functions of amyloid precursor protein in metabolic diseases.* Metabolism, 2021. **115**: p. 154454.
54. Roth Flach, R.J., et al., *Endothelial protein kinase MAP4K4 promotes vascular inflammation and atherosclerosis.* Nat Commun, 2015. **6**: p. 8995.
55. Hamada, M., et al., *MafB promotes atherosclerosis by inhibiting foam-cell apoptosis.* Nat Commun, 2014. **5**: p. 3147.
56. Hasegawa, H., et al., *The role of macrophage transcription factor MafB in atherosclerotic plaque stability.* Atherosclerosis, 2016. **250**: p. 133-43.
57. Machiya, J., et al., *Enhanced expression of MafB inhibits macrophage apoptosis induced by cigarette smoke exposure.* Am J Respir Cell Mol Biol, 2007. **36**(4): p. 418-26.
58. N, A.G., et al., *Apoptotic cells promote their own clearance and immune tolerance through activation of the nuclear receptor LXR.* Immunity, 2009. **31**(2): p. 245-58.
59. Nonaka, S. and H. Nakanishi, *Microglial clearance of focal apoptotic synapses.* Neurosci Lett, 2019. **707**: p. 134317.
60. Savage, J.C., et al., *Microglial Ultrastructure in the Hippocampus of a Lipopolysaccharide-Induced Sickness Mouse Model.* Front Neurosci, 2019. **13**: p. 1340.
61. Tucsek, Z., et al., *Hypertension-induced synapse loss and impairment in synaptic plasticity in the mouse hippocampus mimics the aging phenotype: implications for the pathogenesis of vascular cognitive impairment.* Geroscience, 2017. **39**(4): p. 385-406.
62. Honer, W.G., *Pathology of presynaptic proteins in Alzheimer's disease: more than simple loss of terminals.* Neurobiol Aging, 2003. **24**(8): p. 1047-62.
63. Counts, S.E., et al., *Synaptic gene dysregulation within hippocampal CA1 pyramidal neurons in mild cognitive impairment.* Neuropharmacology, 2014. **79**: p. 172-9.
64. Spangenberg, E., et al., *Sustained microglial depletion with CSF1R inhibitor impairs parenchymal plaque development in an Alzheimer's disease model.* Nat Commun, 2019. **10**(1): p. 3758.